2018

Heat transfer coefficient, pressure drop, and flow visualization of R1234ze(E), and R1234yf in microchannel tube

Houpei Li
ACRC, the University of Illinois, hli84@illinois.edu

Predrag S. Hrnjak
pega@illinois.edu

Heat transfer coefficient, pressure drop, and flow visualization of R1234ze(E), and R1234yf in microchannel tube

Houpei LI[1], Pega HRNJAK[12*]

[1] ACRC, University of Illinois,
Urbana, Illinois, USA
hli84@illinois.edu

[2]Creative Thermal Solutions, Inc.,
Urbana, Illinois, USA
pega@illinois.edu

* Corresponding Author

ABSTRACT

This paper presents heat transfer coefficient, pressure drop, and flow visualization of R1234ze(E) and R1234yf measured in the same facility as introduced in Li and Hrnjak (2016). Experiments are conducted on a 24-port microchannel tube with a hydraulic diameter of 0.643 mm. Mass flux varies from 100 to 200 kg $m^{-2}s^{-1}$. Heat flux varies from 0 to 6 kW m^{-2}. A comprehensive presentation of measurement will be made in this paper. HTC, PD, and flow pattern will be reported in the same figure. The flow pattern results of R1234yf and R1234ze(E) are shown in the previous paper (Li and Hrnjak, 2018). With the capture of flow pattern, discussion of results are enhanced. The pressure drop of R1234ze(E) is higher than R1234yf. Heat transfer coefficient and flow pattern are similar of the two refrigerants. HTC increases as heat flux or mass flux increases. PD increase as mass flux increases or saturation temperature decreases.

1. INTRODUCTION

A new type of experimental facility for evaluation of heat transfer and hydraulic behavior in microchannel used in this work has been introduced in Li and Hrnjak (2017). Heat transfer coefficients and pressure drops can be measured in one pass simultaneously in the six test sections. In order to further study the two-phase flow in microchannel tube, six visualization sections have been added after each test section on the facility. During the experiments, identical heat flux at the six test sections is set. Six measurements of HTC and six PD are obtained in one pass. Six video of flow pattern are recorded by high-speed camera at the exit of each test section. In this paper, a comprehensive presentation of experimental results is made. Heat transfer coefficient, diabatic pressure drop, real saturation pressure, and flow visualization capture are reported at the same chart.

R134a is tested on the same facility and reported in Li and Hrnjak (2017). R134a and R1234yf has similar pressure at the same saturation temperature. However, they have different reduced pressure, thus different properties. R134a and R1234ze(E) have different reduced pressure and properties. However, HFOs (R1234ze(E) and R1234yf) has much smaller global warming potential than HFC (R134a). According to the 5th IPCC (2014), R134a has a GWP_{100} of 1300, R1234yf has a GWP_{100} of 4.0, and R1234ze(E) has a GWP_{100} less than 1.

Table 1 provided some physical properties of R1234ze(E) and R1234yf at three saturation temperatures. Two-phase heat transfer coefficient is related to surface tension, conductivities, vaporization enthalpy, etc. Two-phase is related to densities, viscosities, etc. Flow pattern is related to surface tension, densities, viscosities, etc. At the same saturation temperature, R1234yf has larger reduced pressure, thus smaller surface tension than R1234ze(E). Due to smaller surface tension, R1234yf has larger nucleate boiling heat transfer coefficient. R1234ze(E) has larger vaporization enthalpy and liquid conductivity, which are benefit to higher HTC. R1234yf has smaller vapor density and liquid-to-vapor densities ratio, which are benefit to lower pressure drop.

Table 1. Comparison of R1234ze(E), and R1234yf of physical properties at three saturation temperatures.

Property	Unit	R1234ze(E)			R1234yf		
P_{sat} (T_{sat})	kPa (°C)	427.4 (20)	578.4 (30)	766.5 (40)	437.5 (10)	591.7 (20)	783.5 (30)
P_R	-	0.118	0.159	0.211	0.129	0.175	0.232
σ	mN m^{-1}	9.500	8.210	6.956	8.100	6.798	5.564
H_{lv}	kJ kg^{-1}	170.5	162.9	154.8	156.6	149.3	141.2
k_l	W $m^{-1}K^{-1}$	0.0761	0.0727	0.0692	0.0698	0.0682	0.0620
k_v	W $m^{-1}K^{-1}$	0.0132	0.0141	0.0150	0.0125	0.0133	0.0144
Cp_l	kJ $kg^{-1}K^{-1}$	1.366	1.406	1.443	1.327	1.369	1.416
Cp_v	kJ $kg^{-1}K^{-1}$	0.959	1.007	1.051	0.972	1.023	1.086
ρ_l	kg m^{-3}	1179	1146	1112	1144	1110	1073
ρ_v	kg m^{-3}	22.61	30.52	40.64	24.27	32.80	43.73
$\mu_l/10^{-4}$	kg $m^{-1}s^{-1}$	2.116	1.880	1.670	1.845	1.637	1.453
$\mu_v/10^{-4}$	kg $m^{-1}s^{-1}$	0.1202	0.1246	0.1293	0.1046	0.1087	0.1135
Pr_l	-	3.796	3.625	3.483	3.590	3.445	3.319
Pr_v	-	0.875	0.893	0.909	0.814	0.832	0.857

2. FACILITY AND DATA REDUCTION

2.1 Overview of the Facility

The experimental facility has been firstly introduced in Li and Hrnjak (2016) to study heat transfer and hydraulic behavior of refrigerants in microchannel tubes. The facility can measure heat transfer coefficient for a given heat flux, mass flux, and wall temperature. In the meantime, diabatic pressure drop and flow regime at exit of each test section can be collected. Adiabatic pressure drop can be measured separately without heat load. The facility is made of 3 loops: refrigerant loop, coolant loop, and chiller loop, as shown in Figure 1.

Starting from the oil sampler in refrigerant loop, subcooled refrigerant is pumped by a gear pump at upstream of the oil sampler and moving to a Micro Motion CMF010 mass flow meter (Emerson, 2017). A 2 kW heater controlled by Din-A-Mite (WATLOW, 2016) is used to heat the refrigerant to a certain temperature at the inlet of test line. The test line consists of one precisely controlled evaporator and five conditioning sections to set the inlet condition of the following test section, and six test sections for heat transfer and pressure drop measurements as shown in the top of the refrigerant loop in Figure 1. In the test line, heat transfer blocks are used to transfer heat to refrigerant. Both evaporation and condensation experiments can be done on the same facility because heat is exchanged by water heating or cooling.

A heat transfer block is 152.4 mm long and with water channel inside for coolant loop. Two blocks sandwich a microchannel tube and the wall temperature is measured by six inserted thermocouple probes placed in wells near the tube in each block. Two blocks are tightened by four long screw bolts with nuts with the same torque (7.6 N-m). Between the blocks and microchannel, the surface cavities are filled with thermal paste CHEMPLEX 1381 DE (LUBRITECH, 2007) with reported thermal conductivity with 0.75 W-$m^{-1}K^{-1}$. In each test section, the microchannel tube is 181.8 mm long combined with heated length (152.4 mm) and the rest in connectors. After the test section, refrigerant goes through visualization section and conditioning section. The conditioning section has the same design of test section but longer in length (400 mm), without wall temperature TC well, and is not tightened. The heat transfer rate of the test or conditioning section is determined by the flow rate of coolant into the heat transfer block and the temperature difference of coolant at the outlet and inlet of the block. Only in test sections, the top and bottom blocks have different controls to make sure the conditions from top and bottom side to the microchannel tube are the same. Two sets of flow meter, valve, heater, and thermocouple control the top and bottom heat transfer blocks individually.

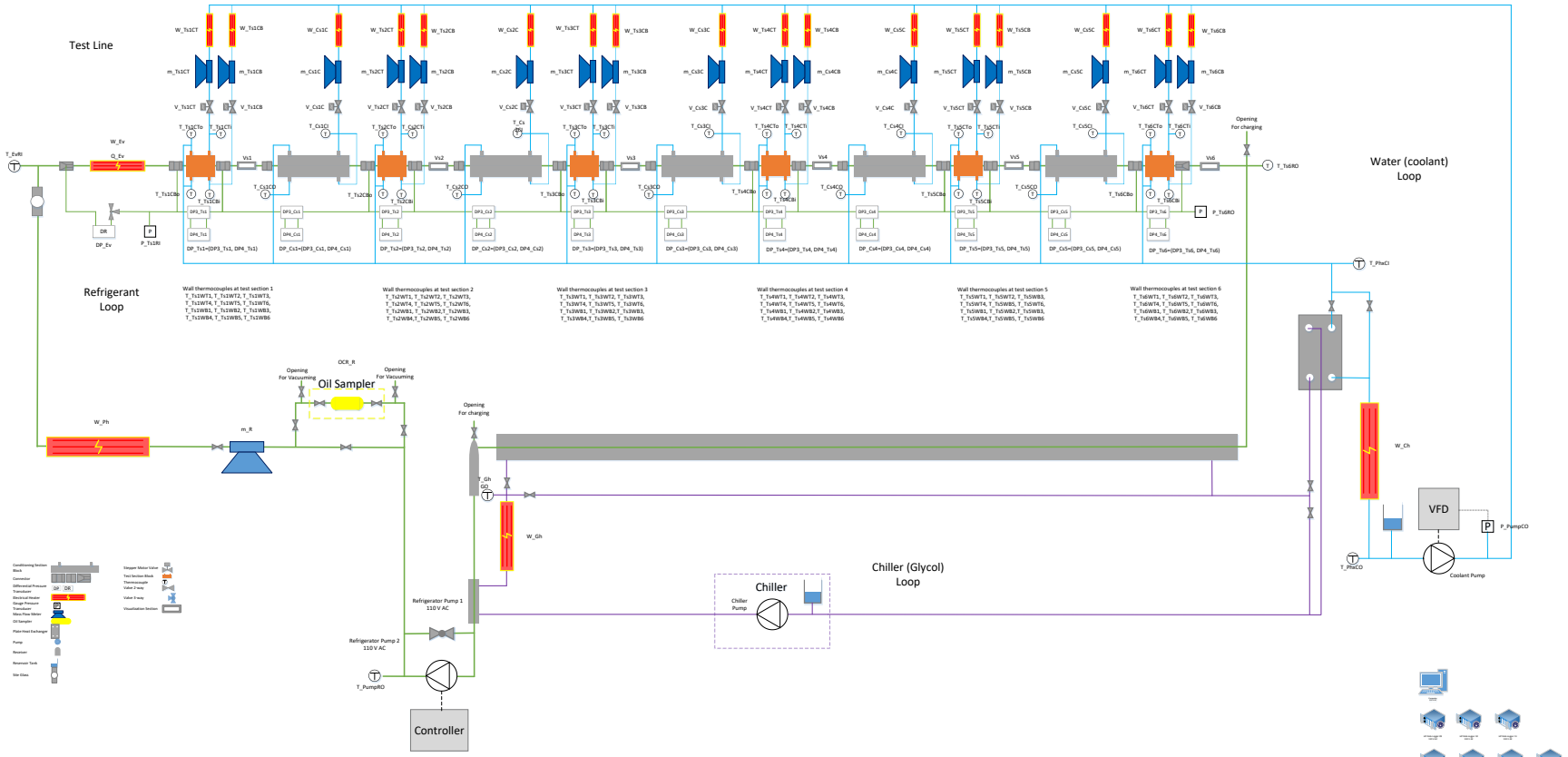

Figure 1. Schematic of the facility with refrigerant loop (green), coolant loop (blue), and chiller loop (purple).

Heat transfer rate combined with refrigerant mass flow rate and pressure determines the increase in vapor quality within the conditioning section. Saturation pressure or temperature is determined by adding (or subtracting) pressure drop in each section. On each pressure measurement point, there are two Rosemount pressure transducers with different range and accuracy for the measurement. The two-pressure-sensor-design provides excellent and needed accuracy of both absolute and differential pressure measurements over the range of operation wider that the range of a single sensor. On one test section, a pair of Rosemount 1151 DP3 (Rosemount, 2008) (range = 2 kPa, εDP = 0.002 kPa) and DP4 (range = 15 kPa, εDP = 0.015 kPa) differential pressure transducers are installed. The sensor with higher range is used when the measured value beyond the limit of the sensor with lower range. When all pressure drops are added together, it should be equal to the difference between the readings of pressure transducers at the inlet and outlet of the test line, within the accuracy. With a proper control, six measurement conditions of quality changes required are taken simultaneously over the full range from 0 to 1, at the same mass flux and adjusted to be the same heat flux. So, six heat transfer coefficients and pressure drops are measured at the same time.

After the test line, a lab-made coaxial (microchannel in a round tube) heat exchanger and a shell-and-tube sub-cooler is used to condense the refrigerant. Openings located at the inlet and outlet of test line is for charging and evacuation. An external receiver is used to help setting up the system pressure. Oil sampler is by-passed at this stage since a pure refrigerant is being tested. The oil sampler will be used to measure oil circulation rate when testing refrigerant-oil mixtures in the future.

Distilled water in the coolant loop is pumped by a cylindrical pump to a heater. When a lower temperature is needed water in the coolant loop could be replaced by ethanol or glycol mixture. A pump with VFD controller is used to pump the fluid. A reservoir tank is installed at the suction of the pump in order to maintain a minimum suction pressure. The pressure at the discharge is measured by a pressure sensor and this signal is used to adjust the pump speed to maintain discharge pressure. Fluid is supplied to an inlet header from where it goes to each test/conditioning section. The fluid temperature at the inlet to the test or conditioning section is adjusted by a 530 W heater while the flow rate is adjusted by a stepper motor valve. The mass flow rate is measured by two CMF010 mass flow meters per test section (heat transfer in upper and lower blocks are measured independently) and a DS006 mass flow meter per conditioning section. Temperature is measured by T-type thermocouple probes inserted into the coolant tube. Coolant from test sections and conditioning sections returns to the outlet header. A plate heat exchanger and a 1.5 kW heater are installed after the header to adjust coolant temperature supplied to the pump.

The chiller loop provides cooling to the refrigerant sub-cooler, refrigerant condenser, and brazed plate heat exchanger in the coolant loop. The chiller loop consists of a chiller with pump and reservoir tank and now is running with 50%-50% ethylene-glycol water mixture. After the pump, glycol flows to a sub-cooler which sub-cools the refrigerant to make sure that liquid refrigerant flows into the gear pump. A 1.5 kW heater is used to adjust the condenser inlet temperature of glycol. A bypass has been made for the condenser to reduce pressure drop when the system is in condensation mode. A plate heat exchanger is used for glycol so that the coolant loop can be cooled.

More detailed description of the facility can be found in Li and Hrnjak (2017) and Li (2016). The details of visualization section can be found in Li and Hrnjak (2018).

2.2 Calibration Process

Instruments are calibrated to make sure the accuracy of measurements. The overall uncertainties of instruments are listed in Table 2.

Table 2. Uncertainties of instruments.

εP	1.25 kPa
εDP	0.0015 to 0.04 kPa
εT	0.07 to 0.2 °C
εm	0.1% to 0.15% of rate
ερ	0.0005 g-cm^{-3}

Heat transfer between the system and ambient is measured and the heat transfer rate from the water side to the refrigerant side is corrected based on the calculated UA. UA is measured by running single-phase refrigerant and water at the same temperature. Heat transfer measured in the water loop is the heat loss since most of the microchannel tube is covered by heat transfer block. Total heat gain in the refrigerant side is calculated from enthalpy difference of the sub-cooled refrigerant at inlet and super-heated at outlet of the test line. The total heat transferred in the water side is

calculated from water capacity and temperature difference at inlet and outlet. 50 comparisons between the total heat transferred in refrigerant and water sides shows before correction, the difference is less than 11% based on refrigerant side. After applying the correction, the difference between heat gain in refrigerant side and the heat transferred in water side is always less than 4.8%.

The contact resistance between heat transfer block to the microchannel tube is measured and the value is 0.0086 K W^{-1}, see Li and Hrnjak (2017). The difference between measured heat transfer coefficients with and without considering the contact resistance can be about 10-20%.

Tube channel size is measured by Mitutoyo WF microscope. The average diameter of the 24 channels is 0.643 mm, and the standard deviation of diameters is 0.0232 mm. Based on the drawing provided by the tube manufacturer, the total perimeter of 24 channels is 7.161×10^{-2} m, the total cross-sectional area is 1.076×10^{-5} m^2. Based on the measurement, the perimeter is 4.961×10^{-2} m, and the cross-sectional area is 7.968×10^{-6} m^2 instead. In the drawing, ports are rectangle with an aspect ratio of 0.616. However the single phase laminar frictional agrees with round tube behavior that fanning fRe equals to 16.

Detailed calibration process and channel size measurement can be found in previous study (Li and Hrnjak, 2016) and the thesis (Li, 2016).

2.3 Data Reduction

Heat transfer coefficient (HTC in kW-$m^{-2}K^{-1}$) is determined based on the wall temperature:

$$HTC = \frac{Q}{A_s(T_{wall} - T_{ref})} \tag{1}$$

In equation 2, A_s is the total port surface area (multiply 24 ports' parameters and the length of tube). T_{wall} is a corrected wall temperature considered the conductive and contact resistance. T_{ref} is the bulk refrigerant temperature and is calculated from the average saturation pressures of the inlet and outlet of the test section. By using the average value, the pressure along the microchannel tube is assumed linear. This is valid if the condition is assumed to be quasi-local. Q is the total heat transfer rate measured in the coolant loop based on the flow rate and the temperatures at inlet and outlet of the block for known specific heat of the secondary (heating) fluid. Q is then corrected with heat transferred between the system and ambient.

$$PD = \frac{DP}{L} \tag{2}$$

The pressure drop gradient (PD in kPa-m^{-1}) is determined by dividing differential pressure measurement and the length of the tube, shown in equation 3.

$$x = f\left(\frac{P_{in,sat} + P_{out,sat}}{2}, \frac{H_{in,sat} + H_{out,sat}}{2}\right) \tag{3}$$

Local vapor quality is calculated based on average saturation pressure and enthalpy. By using the average value of the inlet and outlet of the test section, the pressure and enthalpy along the microchannel tube is assumed to be linear. This is valid when pressure drop and heat transfer rate are constant along the tube. In diabatic condition, the vapor qualities difference between the inlet and outlet of one test section is mainly contributed by enthalpy change. In adiabatic condition, qualities have a slight difference due to pressure drop.

Based on NIST technical Note 1297 (Taylor and Kuyatt, 1994), the overall uncertainty (εR) of a result (R) with a known function F of n variables x_i with known uncertainties (εx_i) could be expressed in equation 4. This equation is under assumptions that all variables are independent, repeated measurements show Gaussian distribution, and all uncertainties of variables are in the same level of confidence. In this paper, the level of confidence is 95%.

$$\varepsilon R = \sqrt{\sum_{i=1}^{n}\left(\frac{\partial F}{\partial x_i}\varepsilon x_i\right)^2} \tag{4}$$

3. EXPERIMENTAL RESULTS

3.1 Adiabatic Pressure Drop

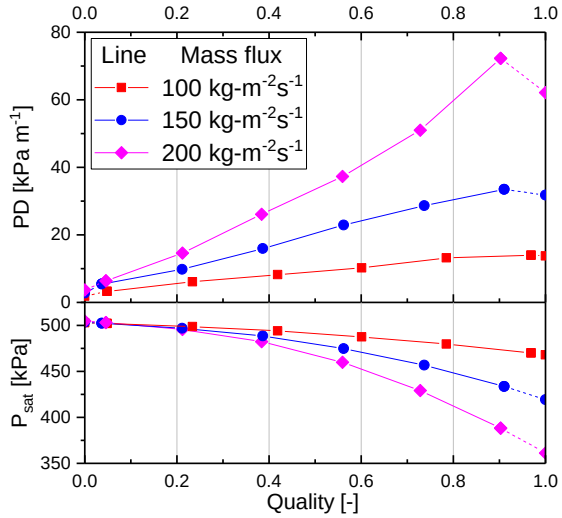

Figure 2. Two-phase pressure increases as mass flux increases. (Adiabatic condition, inlet T_{sat} is 25 °C. Single-phase points are calculation based on Churchill, 1977)

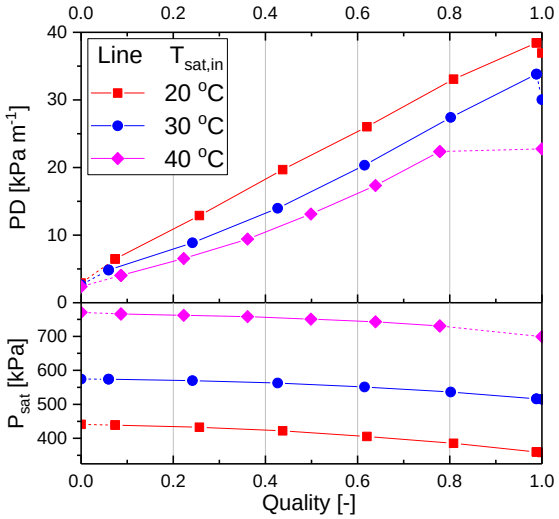

Figure 3. Two-phase pressure drop increases as the saturation pressure decreases. (Adiabatic condition, mass flux is fixed at 150 kg $m^{-2}s^{-1}$. Single-phase points are calculation based on Churchill, 1977)

Two-phase pressure drop is measured first in adiabatic condition. From test section 1 to 6, the actual saturation pressure is decreasing due to pressure drop (non-isobaric condition). In each figure, three group of data with six qualities are obtained from experiment (connected with solid line). Pressure drop in the plots at quality 0 and 1 (connected with dash line) are prediction from Churchill (1977) and the properties are evaluated at the saturation pressure that calculated from a third-order curve fitting of the real pressure (connected with dash line).

The two-phase pressure drop of R1234ze(E) increases as the vapor quality increases, as Figures 2 and 3 shows. Started from liquid phase, refrigerant is evaporated and becomes to two-phase flow. At low quality, the flow is plug/slug flow. The plug/slug flow has the interphase velocity and vapor fraction agrees to the results of homogeneous flow. As quality increases, the velocity of the flow increases. Liquid slug disappears in the channel, and liquid ring or bridge is observed instead. Higher void fraction makes the flow velocity higher and overall viscosity lower, due to vapor has lower density and viscosity, consequently increases the pressure drop. At high quality, the flow becomes annular with film or even waves. The waves and instability happen at the interphase dissipate energy and consequently increases the pressure drop.

As the mass flux increases, the two-phase pressure increases. The shape of the pressure drop curves changes: at mass flux of 100 kg-$m^{-2}s^{-1}$, the curve concave down; at mass flux of 200, the curve concave up. The reason is that at higher mass flux, there is more waves at annular flow which dissipates the energy. At lower mass flux, the annular flow has less waves or even no wave. The other reason comes from saturation pressure changes. At higher mass flux, the actual saturation pressure is lower at high vapor quality. As the saturation pressure is lower, the pressure drop is higher, as shown in Figure 3. At lower saturation pressure, low vapor density increases the velocity of vapor as Table 1 shows. The densities ratio between liquid and vapor is higher which increases the slip ratio and the waviness.

3.2 Effect of Mass Flux

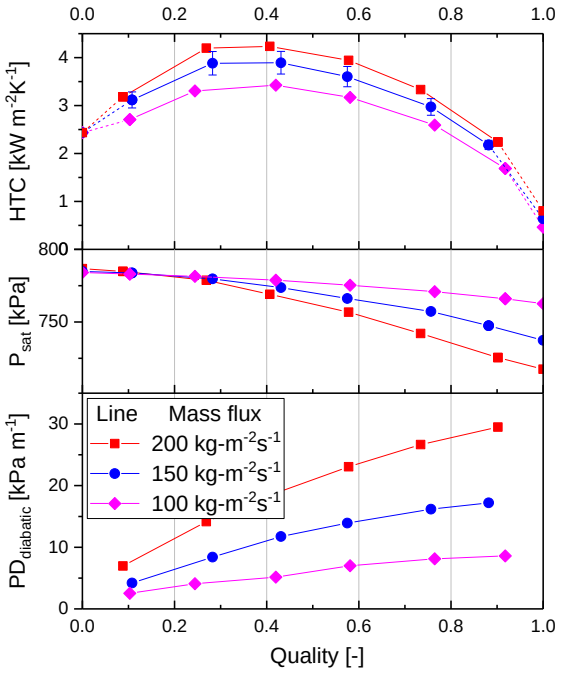

Figure 4. Heat transfer coefficient of R1234ze(E) increases as mass flux increases. (Fixed heat flux at 4 kW m^{-2}, inlet T_{sat} is 25 °C. Liquid-phase points are calculation based on Gorenflo and Kenning (2010). Vapor-phase points are calculation based on Dittus-Boelter.)

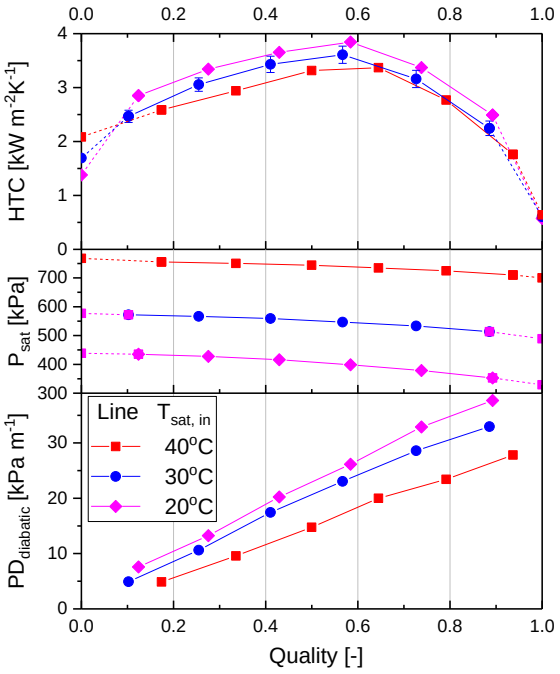

Figure 5. Heat transfer coefficient changes as inlet saturation temperature changes. (Fixed mass flux at 150 kg $m^{-2}s^{-1}$, heat flux at 4 kWm^{-2}. Liquid-phase points are calculation based on Gorenflo and Kenning (2010). Vapor-phase points are calculation based on Dittus-Boelter.)

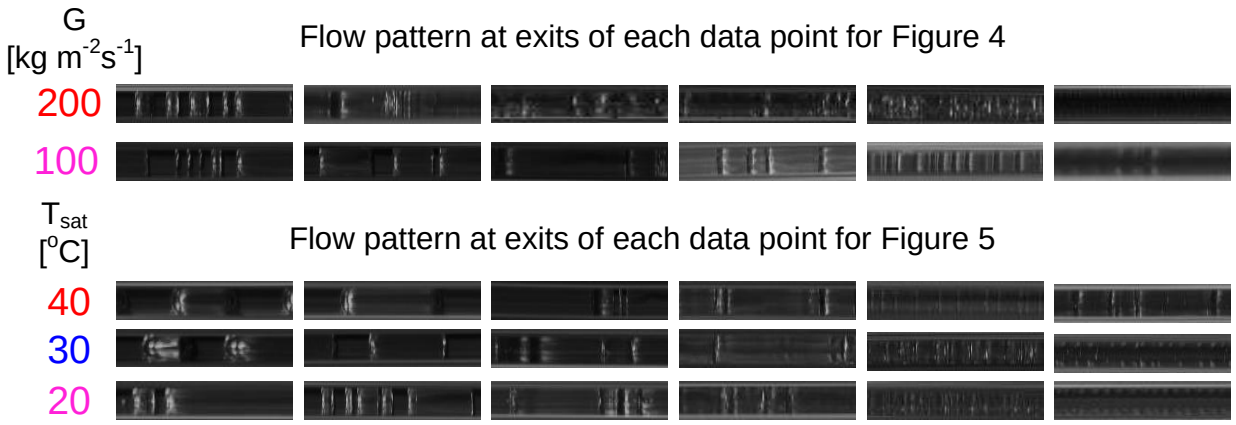

Figure 6. Flow pattern captures at exits of measurements in Figures 4 and 5.

Figure 4 shows that heat transfer coefficient of R1234ze(E) increases as quality increases. Flow pattern captures at exist of mass fluxes from 100 to 200 kg-$m^{-2}s^{-1}$ are presented in Figure 6. At mass flux of 100 kg-$m^{-2}s^{-1}$, the plug/slug flow pattern continues until quality of 0.6. Transitional flow pattern happens at higher quality where the boundary of plug is not clear anymore. We observed dark regions at mass flux of 100 at moderate quality which is a thick liquid ring or vapor bridge. In the last picture, a liquid film with some waves is observed. At mass flux of 200 kg-$m^{-2}s^{-1}$, the flow is much wavier than the case of 100 kg-$m^{-2}s^{-1}$. Unclear plug boundary occurs at the second picture, where the exit quality is only 0.3. At the fifth picture, where is the local maximum of HTC, there is a very wavy annular flow.

At the plug/slug flow, HTC increases as the quality increases by the help of increasing velocity. HTC reaches a maximum at vapor quality of about 0.5 at mass fluxes 100 and 150 kg-m^{-2}s^{-1}. At mass flux of 200, the local maximum of HTC moves to higher quality (0.7) due to larger convective heat transfer effect. Comparing the flow pattern at quality of 0.7, there is more waves when mass flux is 200 than 100 kg-m^{-2}s^{-1}. The wave extends the annular flow pattern to higher quality and reduces the chance of partially dry-out.

As the mass flux is doubled from 100 to 200 kg-m^{-2}s^{-1}, the HTC increases about 15% overall. However, the pressure drop is about six times higher since pressure drop has high sensitivity to velocity at small diameter. As mass flux increase, the shape of curve of pressure drop in the plot changes from concaves down to up.

3.3 Effect of Saturation Temperature

Figure 5 shows that a lower saturation temperature gives a higher heat transfer coefficient. Flow pattern captures at exist of saturation temperature at 20, 30, and 40 ^{o}C are presented in Figure 6. The difference among flow pattern of three saturation temperature is small. Plug/slug flow pattern occurs at the first two data point, where quality is lower than 0.6. Then the flow gets unstable and transitional flow pattern occurs. In the last picture, where quality is about 0.9, there is a difference that for case of saturation temperature inlet of 40 ^{o}C, the flow is still in transitional that the dark liquid region still occurs. However, for the cases of 20 and 30 ^{o}C, the flow is already annular. In table 1, it shows that as saturation temperature increase, the vapor density increase. So, the vapor velocity will decease and further extend the flow pattern of transitional to higher quality.

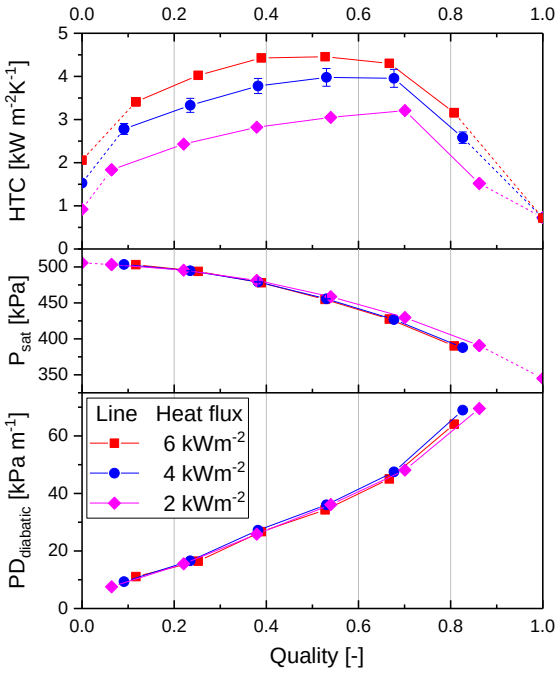

Figure 6. Heat transfer coefficient of R1234ze(E) increases as heat flux increases. (Fixed mass flux at 200 kg m^{-2}s^{-1}, inlet T_{sat} is 25 ^{o}C. Liquid-phase points are calculation based on Gorenflo and Kenning, 2010. Vapor-phase points are calculation based on Dittus-Boelter.)

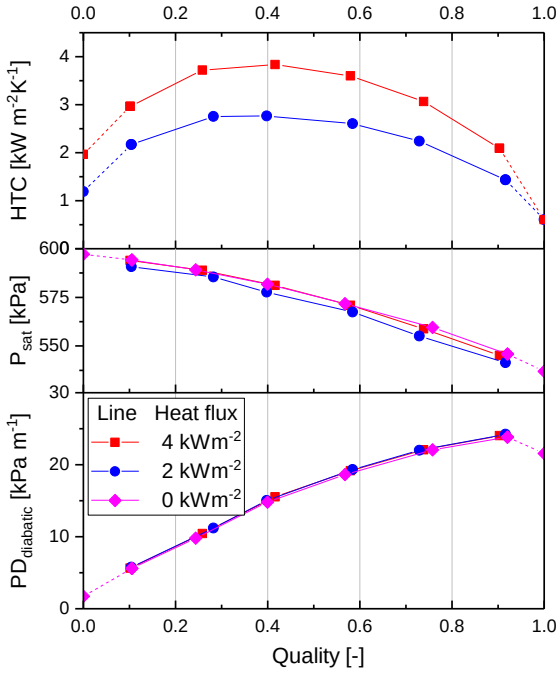

Figure 7. Heat transfer coefficient of R1234yf increases as heat flux increases. (Fixed mass flux at 150 kg m^{-2}s^{-1}, inlet T_{sat} is 30 ^{o}C. Liquid-phase points are calculation based on Gorenflo and Kenning, 2010. Vapor-phase points are calculation based on Dittus-Boelter.)

According to Gorenflo's prediction (Gorenflo and Kenning, 2010), high saturation temperature should have a higher nucleate boiling HTC due to lower surface tension. As we connect the first data point at lowest quality to the prediction, a trend is found that the HTC is higher at very low quality (less than 0.1) when saturation temperature is higher. As saturation temperature increases, the ratio of liquid to vapor densities decrease which reduces the waviness effect and connective HTC.

3.4 Effect of Heat Flux

The heat flux has significant effect on heat transfer coefficient, as Figures 6 and 7 show. Started from the single-phase refrigerant, the Gorenflo and Kenning (2010) predicts the magnitude of nucleate boiling HTC at low quality. As the heat flux increase, the nucleate boiling HTC increase. Heat transfer coefficient measurements at two-phase basically follows the prediction's magnitude, but higher than the prediction. This may due to underestimate of Gorenflo: it measures the boiling effect for outer surface and has a database with much higher heat flux than the experimental conditions in this work. Another reason is that the convective heat transfer increases the HTC. When quality close to 1, two-phase HTC should be close to the single-phase vapor HTC. In Figures 6 and 7, Dittus-Boelter is used to predict single-phase HTC and plotted. Singe-phase HTC is a function of mass flux and properties, so it is not affected by heat flux.

Both frictional and accelerating pressure drop contribute to the total diabatic pressure drop. From Figures 7 and 8, the total pressure drop at varies heat flux are similar. The accelerating effect is small relative to the frictional pressure drop. Comparing Figures 6 and 7, the accelerating effect of R1234ze(E) is larger than R1234yf. According to Table 1, R1234ze(E) has larger liquid-to-vapor densities ratio, thus the effect of volume expansion is larger.

4. SUMMARY AND FUTURE WORK

Two-phase HTC and pressure drop of R1234yf and R1234ze(E) in a 0.643 mm 24 parallel-port microchannel tube have been measured and reported. Visualization results are reported with HTC and PD for further discussion.

Two-phase pressure drop increases as mass flux increases or saturation temperature decreases. Physical properties have larger effect on PD rather than flow pattern according to Table 1 and Figure 6. Heat flux has relatively insignificant effect on pressure drop. Higher mass flux or heat flux both lead to a higher heat transfer coefficient. When mass flux is higher, wavier flow is observed at higher quality, which is one of the causes that HTC is enhanced. Based on Gorenflo and Kenning (2010), nucleate boiling HTC is higher when heat flux is higher. As saturation temperature decrease, two-phase HTC increases. Flow pattern affects HTC and PD. The waviness in annular flow increases the HTC and PD. When flow is transitioning from plug/slug flow to annular flow, the HTC is higher.

Further research on expanding conditions and refrigerants is ongoing. Upcoming publications will present heat transfer coefficient, pressure drop, and flow characteristics of new refrigerants. Blends with low GWP refrigerant or oil mixtures will be included in the future. Condensation experiments will also be conducted on this facility.

NOMENCLATURE

A	Area	m^2
Cp	Thermal capacity	kJ $kg^{-1}K^{-1}$
D	Diameter	m
DP	Differential pressure	kPa
G	Mass flux	kg-$m^{-2}s^{-1}$
GWP_{100}	100-year direct global warming potential	-
H	Enthalpy	kJ kg-1
HTC	Heat tranfser coefficient	kW-$m^{-2}K^{-1}$
J	Superficial velocity	m-s^{-1}
k	Thermal conductivity	W $m^{-1}K^{-1}$
L	Length	m
P	Pressure	kPa
PD	Pressure drop	kPa-m^{-1}
P_R	Reduced pressure	-
Q	Heat transfer rate	kW
Q''	Heat flux	Wm^{-2}
T	Temperature	K
x	Vapor quality	-

Greek leters		
ε	Uncertainty	-
μ	dynamic viscosity	Pa-s
ρ	density	kg m-3
σ	surface tension	N m-1

Subscript

l	Liquid
lv	Liquid to vapor
ref	Refrigerant
s	Surface
sat	Saturation
v	Vapor
wall	Wall

REFERENCES

Churchill, S. W. (1977). Friction-factor equation spans all fluid-flow regimes. *Chemical Engineering*.

Emerson (2017). Micro Motion® ELITE® Coriolis Flow and Density Meters. Product Data Sheet PS-00374, Rev AE (July 2017).

IPCC, 2014: Climate Change 2014: Synthesis Report. (2014). Geneva, Switzerland: Contribution of Working Groups I, II and III to the Fifth Assessment Report of the Intergovernmental Panel on Climate Change [Core Writing Team, R.K. Pachauri and L.A. Meyer (eds.)].

Gorenflo, D., & Kenning, D. (2010). Pool Boiling. *VDI Heat Atlas* (2nd ed., pp. 757–788). Springer.

Li, H. (2016). An Experimental Facility for Microchannel Research and Evaporating R134a in Microchannel Tube. University of Illinois.

Li, H., & Hrnjak, P. (2016). Heat Transfer and Pressure Drop during Evaporation of R134a in Microchannel Tubes. International Compressor Engineering, Refrigeration and Air Conditioning, and High Performance Buildings Conferences (pp. 1–10).

Li, H., & Hrnjak, P. (2017). Measurement of heat transfer coefficient and pressure drop during evaporation of R134a in new type facility with one pass flow through microchannel tube. International Journal of Heat and Mass Transfer, 115, 502–512. Elsevier Ltd.

Li, H., & Hrnjak, P. (2018). Flow Visualization of R134a, R1234ze(E), and R1234yf in microchannel tube. International Compressor Engineering, Refrigeration and Air Conditioning, and High Performance Buildings Conferences.

LUBRITECH (2007). CHEMPLEX® 1381 Product Information. (March 26th 2007)

Rosemount (2008). Rosemount 1151 Pressure Transmitter. Reference Manual 00809-0100-4360 (August 2008).

Taylor, B. N., & Kuyatt, C. E. (1994). Guidelines for Evaluating and Expressing the Uncertainty of NIST Measurement Results. Technology.

WATLOW (2016). DIN-A-MITE® Solid-State Power Controller User's Manual. (January 2016).

ACKNOWLEDGEMENT

This paper is a result of a project that was financially supported by the Air Conditioning and Refrigeration Center at the University of Illinois and its 30 member companies. CTS (Creative Thermal Solutions Inc.) provided complete technical support like material, instrumentation and previous 3 m long facility as a basis for the new, enlarged and improved facility used to acquire presented data. Authors also acknowledge support of Honeywell in providing the refrigerant R1234ze(E) and R1234yf.